MNRAS **000**, 1–10 (2016) Preprint 26 August 2016 Compiled using MNRAS LATEX style file v3.0

A wind-driving disc model for the mm-wavelength polarization structure of HL Tau

Titos Matsakos,* Petros Tzeferacos and Arieh Königl
Department of Astronomy & Astrophysics, The University of Chicago, 5640 S. Ellis Ave, Chicago, IL 60637, USA

arXiv:1608.06960v1 [astro-ph.SR] 24 Aug 2016

Accepted XXX. Received YYY; in original form ZZZ

ABSTRACT

The recent advent of spatially resolved mm- and cm-wavelength polarimetry in protostellar accretion discs could help clarify the role of magnetic fields in the angular momentum transport in these systems. The best case to date is that of HL Tau, where the inability to produce a good fit to the 1.25-mm data with a combination of vertical and azimuthal magnetic field components was interpreted as implying that centrifugally driven winds (CDWs) are probably not a significant transport mechanism on the $\sim 10^2$ au scale probed by the observations. Using synthetic polarization maps of heuristic single-field-component discs and of a post-processed simulation of a wind-driving disc, we demonstrate that a much better fit to the data can be obtained if the radial field component, a hallmark of the CDW mechanism, dominates in the polarized emission region. A similar inference was previously made in modelling the far-infrared polarization map of the pc-scale dust ring in the Galactic centre. To reconcile this interpretation with theoretical models of protostellar discs, which indicate that the wind is launched from a comparatively high elevation above the mid-plane, we propose that most of the polarized emission originates – with a high ($\gtrsim 10\%$) intrinsic degree of polarization – in small ($\lesssim 0.1$ mm) grains that remain suspended above the mid-plane, and that the bulk of the mm-wavelength emission is produced – with low intrinsic polarization – by larger grains that have settled to the mid-plane.

Key words: magnetic fields – polarization – protoplanetary discs – stars: individual: HL Tau – ISM: jets and outflows – submillimetre: planetary systems

1 INTRODUCTION

Magnetic fields are thought to be crucial to the transport of angular momentum in accretion discs, but the precise nature of their effect is still an open question. The two leading scenarios that have been debated in the literature both require an ordered, large-scale field (characterized by a thermal-to-magnetic pressure ratio β) to be present. In one picture, the transport takes place in the plane of the disc either through MHD turbulence that is induced by the magnetorotational instability (MRI; e.g. Balbus 2011) or, if the field is strong enough, through large-scale correlations in a laminar flow (e.g. Simon et al. 2013); in this case $\beta_0 \gg 1$ (where the subscript 0 denotes the mid-plane). In the alternative scenario, angular momentum is transported vertically through the disc surfaces in the form of a centrifugally driven wind (CDW; e.g. Königl & Salmeron 2011); it is efficient only if β_0 is not $\gg 1$. It was, however, realized early on (Li 1996; Wardle 1997) that, in the case of weakly ionized discs where the field–matter coupling near the mid-plane is weak, a CDW can dominate the angular momentum transport even if $\beta_0 \gg 1$. In such discs, the wind is launched from a comparatively high elevation (a few thermal-pressure scale heights above the mid-plane), where ionizing radiation from an external source can penetrate the disc and ensure good coupling. It was subsequently also realized (Salmeron et al. 2007) that both mechanisms can in principle operate at the same radial location in the disc – with radial transport dominating closer to the mid-plane and vertical transport becoming important at a height where the density (and, correspondingly, β) is sufficiently low for the magnetic field to suppress the MRI and drive a wind. Recent numerical simulations of $\beta_0 \gg 1$ protoplanetary discs have indicated that high-elevation CDWs arise naturally in such systems – even if the mid-plane coupling remains adequate – and that they can potentially play a role in the angular momentum transport all along the disc, with radial transport contributing to varying degrees at lower disc elevations (e.g. Bai & Stone 2013; Bai 2013; Simon et al. 2013; Lesur et al. 2014; Bai 2015; Gressel et al. 2015; Simon et al. 2015).

The continuum radiation of molecular discs is dominated by the thermal emission of dust. This emission will be

* E-mail: titos.matsakos@uchicago.edu

© 2016 The Authors

polarized if non-spherical dust grains become aligned with respect to the local magnetic field. Various mechanisms can potentially effect such an alignment, with radiative torque (e.g. Draine & Weingartner 1996) being a favoured possibility for protoplanetary discs. If the polarized emission can be spatially resolved, it may be used to probe the magnetic field structure in such discs (e.g. Cho & Lazarian 2007) and potentially shed light on the angular momentum transport process.

Molecular accretion discs are found not just in protostars but also – on much larger scales – in galactic nuclei, both active (e.g. Tristram et al. 2014) and quiescent. In fact, the first polarimetric observations of such a disc were carried out at far-infrared ($\sim$100 μm) wavelengths for the pc-scale dust ring in the Galactic centre (Hildebrand et al. 1990, 1993). The data for this disc, which is observed at a fairly large inclination angle ($i \approx 70^\circ$), could be interpreted in terms of radial (r) and azimuthal (ϕ) magnetic field components that are of comparable magnitude but opposite signs, and a relatively weak vertical (z) field component, consistent with the expectations for a weakly ionized disc in which a CDW dominates the angular momentum transport (Wardle & Königl 1990).

It has now also become possible to resolve the magnetic field structure of protoplanetary discs through interferometry at sub-mm to cm wavelengths. Data are already published for the young (Class-I/II) source HL Tau (1.25 mm; Stephens et al. 2014) and for three Class-0 protostars: IRAS 16293-2242B (878 μm; Rao et al. 2014), L1527 (1.3 mm; Segura-Cox et al. 2015) and IRAS 4A (8.1 mm and 1.03 cm; Cox et al. 2015). In contrast to HL Tau, the even younger Class-0 sources are deeply embedded within an extended envelope that can contribute significantly to the observed emission (e.g. Looney et al. 2000). Furthermore, the gravitational collapse of such envelopes may create magnetized pseudo-disc structures that are not genuine (i.e. rotationally supported) discs (e.g. Hennebelle & Ciardi 2009). In the unambiguous case of the HL Tau disc ($i \approx 47^\circ$), Stephens et al. (2014) attempted to fit the data with a combination of azimuthal and vertical field components. They found that, while a pure-B_ϕ field did not fit the data well, the addition of a B_z component only made the fit worse, which led them to the conclusion that a CDW is probably not the dominant angular momentum transport mechanism on the $\sim$80-au scale probed by their observations. In this connection it is worth noting that the protoplanetary disc simulations discussed in Simon et al. (2013, 2015) and Bai (2015) indicate that, at large ($\gtrsim$30 au) radii, the region near the mid-plane could be either turbulent or laminar (depending on the magnetic field strength and the ionization structure) but that in either case the local field would be dominated by the azimuthal component (essentially because of the strong shear of the Keplerian velocity field; cf. Eardley & Lightman 1975). Another noteworthy fact is that in HL Tau there is evidence not just for a central high-velocity jet (e.g. Mundt et al. 1990; Movsessian et al. 2012) but also for an extended, lower-velocity disc wind (e.g. Takami et al. 2007; Lumbreras & Zapata 2014; Klaassen et al. 2016), which is consistent with general expectations for actively accreting protostars (e.g. Ferreira et al. 2006).

In this paper we demonstrate that a considerably better fit to the HL Tau polarization data can be obtained if one also includes the radial field component – which was neglected in the Stephens et al. (2014) analysis – in the modelling. Indeed, we find that the best fit corresponds to $|B_r| \gtrsim |B_\phi| \gg |B_z|$, similar to the result previously obtained for the Galactic-centre disc. (Note, however, that the apparent polarization structures of these two sources are not the same, which can be understood from the difference in their values of the viewing angle i.) Thus, in contradistinction to the inference of Stephens et al. (2014), we find that the polarization data not only do not negate the presence of a CDW in this disc but that they actually support it. The prominence of the radial field component in wind-driving discs is consistent with the requirement that the ratio B_r/B_z at the disc's surface exceed a certain minimum value ($= 1/\sqrt{3}$ for a cold, Keplerian disc; Blandford & Payne 1982) in order for a CDW to be launched.

We complement the modelling approach of Wardle & Königl (1990), who employed a combination of semi-analytic and analytic methods, by using a numerical simulation of a disc with a generic magnetic diffusivity to derive the expected polarization properties of a wind-driving disc. These results are presented in Section 2 and confronted with the HL Tau data in Section 3; in the latter Section we also show synthetic maps for single-component field geometries (pure B_r, B_ϕ and B_z) to help guide the analysis. In Section 4 we discuss our findings in relation to models of the dust distribution in protoplanetary discs and to an alternative interpretation of the data in terms of dust scattering (Kataoka et al. 2015, 2016; Yang et al. 2016a,b); we also comment on the applicability of this model to the observed Class-0 sources. We summarize in Section 5.

2 NUMERICAL MODEL AND SYNTHETIC POLARIZATION MAPS

Our disc model represents the final configuration of a numerical simulation that evolves simultaneously the disc and its outflow, following the approach of Tzeferacos et al. (2009, 2013). We set up a protoplanetary accretion disc that is threaded by a large-scale poloidal magnetic field and is characterized by an isotropic, alpha-type resistivity and an alpha-type viscosity. We integrate the axisymmetric MHD equations (evolving all three vector components in the r–z plane) using the PLUTO code[1] (Mignone et al. 2007, 2012). This model assumes good field–matter coupling throughout the disc, corresponding to the Elsasser number Λ (e.g. Königl & Salmeron 2011) being $\gtrsim 1$ at all heights, as well as $\beta_0 \gtrsim 1$. However, in real protostellar discs, the mid-plane Elsasser number (Λ_0) might drop below 1 and β_0 could be $\gg 1$ on the spatial scales of interest (e.g. Simon et al. 2013, 2015; Bai 2015). Furthermore, the magnetic diffusivity on these scales would be dominated by ambipolar diffusion (with a possible contribution from the Hall term; e.g., Wardle & Koenigl 1993; Bai 2015) and would thus be anisotropic. Nevertheless, as we further elaborate in Section 4, our model should capture the key properties of a

[1] Freely available at: `http://plutocode.ph.unito.it/`

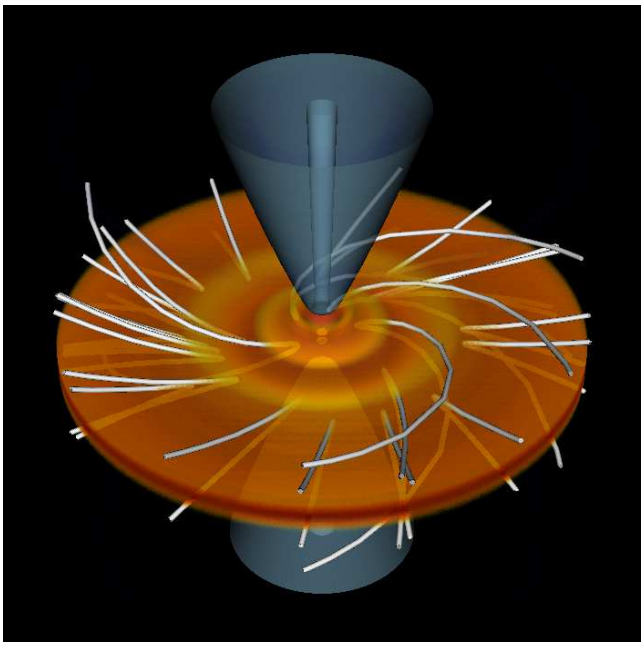

Figure 1. Composite 3D rendering of the disc–wind structure, viewed at an angle of 45°. The orange shading depicts the density distribution in the disc, and the cyan iso-surfaces highlight the central (highest velocity) portion of the wind. (The wind is driven from all disc radii, but its outer portion is not shown.) Also plotted (in white) is a random sampling of magnetic field lines that thread the disc.

wind-driving disc that are germane to its observed polarization structure.

For reference, we adopt the following set of parameters: sound-to-Keplerian speed ratio $e = 0.1$, magnetization $\mu = \beta_0^{-1} = 0.4$, magnetic field inclination parameter $m = 0.3$, magnetic diffusivity parameter $\alpha_m = 0.01$ (with the parameter χ_m being 1, corresponding to full isotropy), and magnetic Prandtl number (the ratio of viscosity to magnetic diffusivity) $\mathcal{P}_m = 1$ (see Tzeferacos et al. 2013 for further details). For these parameter choices, $\Lambda_0 = (2\mu)^{1/2}/\alpha_m \approx 89$. The final outcome of the simulation consists of a self-consistent steady-state disc–wind system, which we reconstruct in 3D for post-processing.

Figure 1 (3D rendering) and the left panel of Fig. 2 (2D vertical slice) show the distribution of the gas mass density ρ and the magnetic field geometry in our model. The distributions of ρ and of the three components of the magnetic field $\boldsymbol{B}$ along a representative field line are plotted in the middle panel of Fig. 2. It is seen that, in this model, the amplitude of the radial field component increases rapidly with height above the mid-plane (where $B_r = B_\phi = 0$), and that, over most of the distance between the mid-plane and the disc surfaces, $|B_r| > |B_\phi| > |B_z|$. In particular, near the disc surfaces, $|B_r/B_z|$ is well in excess of the threshold for the launching of a centrifugally driven wind (see Section 1). In the outflow region above the disc, all field amplitudes decrease with distance along the field line. The behaviour of the ratio $|B_r/B_\phi|$ is similar to the one obtained in semi-analytic models of laminar, strongly coupled wind-driving discs in both the (anisotropic) ambipolar and (isotropic) Ohm diffusivity regimes, for which $|dB_r/dB_\phi|_0 = 2\Lambda_0$ (e.g. Königl et al. 2010).

For the post-processing, we truncate the disc at an outer radius of 175 au and remove the central region (delimited by the inner dashed lines in the left panel of Fig. 2) to avoid integrating through the inner boundary of the simulation. Adopting the disc inclination angle inferred for HL Tau ($i = 46.7°$; ALMA Partnership: Brogan et al. 2015), we generate synthetic polarization maps by considering a virtual detector in the $(\tilde{x}, \tilde{y})$ plane that consists of 16×16 pixels, each associated with a distinct line of sight that intersects the disc–wind structure (dotted lines in the left panel of Fig. 2). Although the 1.3-mm image of the HL Tau disc exhibits a pattern of bright and dark rings, with the latter possibly corresponding to physical gaps, we approximate both the gas and the dust distributions as being smooth, with the dust particle density n_d scaling as ρ. Furthermore, even though the emission from the bright rings is inferred to be at least marginally optically thick at this wavelength (Pinte et al. 2016; Jin et al. 2016), we simplify the analysis by calculating the Stokes parameters in the optically thin limit. Thus we write

$$I = C_\mathrm{I} \int B_\nu n_\mathrm{d}\, \mathrm{d}s\,, \quad \begin{cases} Q = C \int B_\nu n_\mathrm{d} \cos 2\psi \cos^2\zeta\, \mathrm{d}s \\ U = C \int B_\nu n_\mathrm{d} \sin 2\psi \cos^2\zeta\, \mathrm{d}s \end{cases} \tag{1}$$

(e.g. Wardle & Königl 1990), where the integrals are performed along each of the chosen rays. In equation (1), $B_\nu(T_\mathrm{d})$ is the Planck function and T_d the dust temperature, ψ is the angle between the projected magnetic field vector and the $\tilde{y}$ axis (measured counter-clockwise), ζ is the angle between $\boldsymbol{B}$ and its projection on the detector plane, and C, C_I are constants. The quantities within the integrals are all functions of s, with $\mathrm{d}s$ being the line element along the given ray.

For the dust temperature, we follow Stephens et al. (2014) and use the model fit of Kwon et al. (2011) to the mid-plane and surface disc temperatures (subscripts 0 and s, respectively) in HL Tau as functions of the spherical radius R: $T_0 = 190\,(R\,[\mathrm{au}])^{-0.43}\,\mathrm{K}$, $T_\mathrm{s} = 600\,(R\,[\mathrm{au}])^{-0.43}\,\mathrm{K}$. The disc surfaces are taken to be flat, and to be inclined at an angle of 6° to the equatorial plane (black solid lines in the left panel of Fig. 2): these are approximately the loci where the radial velocity changes sign, marking the transition from accretion to outflow. Within the disc the dust temperature is obtained by interpolation, whereas for the wind (subscript w) we assume a higher value, $T_\mathrm{w} = 3T_\mathrm{s}$ (e.g. Bans & Königl 2012). While this temperature distribution favours emission from high latitudes, our assumption that $n_\mathrm{d} \propto \rho$ implies – in view of the strong density stratification (middle panel of Fig. 2) – that the dominant contribution to the total intensity I comes from the mid-plane region.[2] However, as we discuss in Section 4, additional factors may affect the distri-

[2] For $\lambda = 1.25\,\mathrm{mm}$, $B_\nu(T_\mathrm{d})n_\mathrm{d}$ is approximately proportional to $T_\mathrm{d}n_\mathrm{d}$. Since the temperature only changes by a factor of a few over several scale heights, whereas the density exhibits an exponential behaviour, it is n_d that determines the emission. This expectation is confirmed by our results, which are insensitive to the particular choice of T_w.

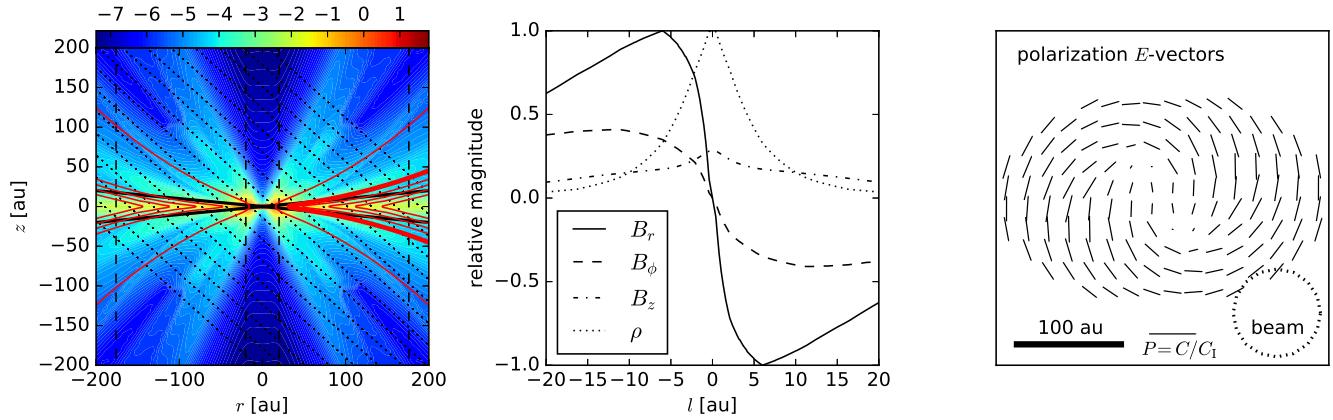

Figure 2. Structure and polarization properties of the simulated disc–wind model. Left panel: vertical slice showing the logarithmic density distribution (colour contours in code units) and the poloidal magnetic field lines (in red). The solid black lines approximate the nominal surfaces of the disc (the locations where the radial velocity component changes sign), the vertical dashed lines delimit the region that is included in the analysis, and the slanted dotted lines represent the directions along which the Stokes parameters are integrated in the application to HL Tau ($i = 46.7°$). Middle panel: gas density and amplitudes of the magnetic field components as functions of projected position (l) along the highlighted (thick red) field line in the left panel. The density is normalized by its mid-plane value whereas the field amplitudes are scaled by the maximum value attained by the dominant (B_r) component. Right panel: predicted polarization map, after convolution with the depicted synthesized beam, for a disc viewed at $i = 46.7°$. The lengths of the plotted E-vectors scale with the degree of polarization P, which is calculated under the assumption that the ratio C/C_I in equation (2) is a spatial constant.

bution of both the polarized and the total dust emissivities in the disc.

Once the Stokes parameters are calculated, we perform a Gaussian convolution ($Q \to Q_{\rm conv}$, $U \to U_{\rm conv}$, $I \to I_{\rm conv}$) using a virtual circular beam of size $0.6''$ (84 au), similar to the one used by Stephens et al. (2014) in HL Tau ($0.65'' \times 0.56''$). The polarization position angle χ and the degree of linear polarization P are then obtained from

$$\tan 2\chi = \frac{U_{\rm conv}}{Q_{\rm conv}} \ , \quad P = \frac{C}{C_{\rm I}} \frac{\left(Q_{\rm conv}^2 + U_{\rm conv}^2\right)^{1/2}}{I_{\rm conv}} \ . \qquad (2)$$

The right panel of Fig. 2 shows the projected electric field vectors for our disc model.[3] We treat the ratio C/C_I as a spatial constant in view of the fact that the shapes and alignment properties of the radiating grains, which determine this ratio, are uncertain. We do, however, take into account the effect on the value of P of cancellations that arise either from the integration along the line of sight or from the beam convolution procedure. Both χ and P vary with position in the disc, reflecting their dependence on the projected field geometry (quantified by the angles ψ and ζ; note that only the component of $\boldsymbol{B}$ that is normal to the line of sight contributes to the polarization) and on the projected distance from the centre of the disc (as the effect of beam averaging is stronger near the centre).

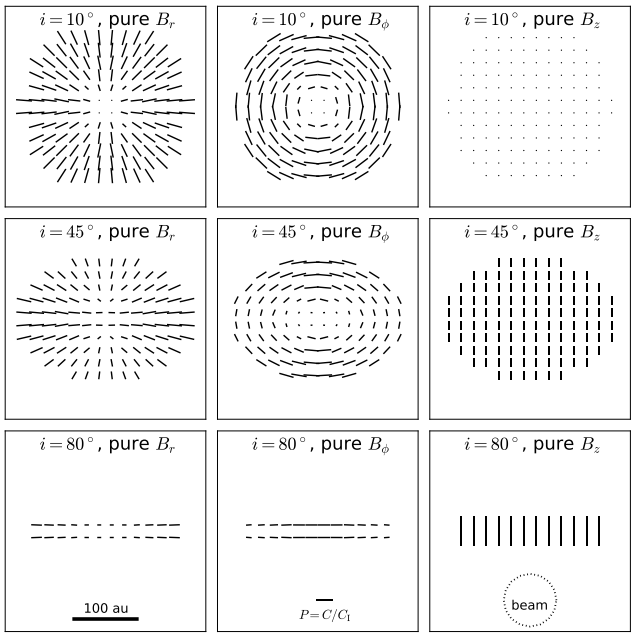
$i = 10°$, pure B_r
$i = 10°$, pure B_ϕ
$i = 10°$, pure B_z
$i = 45°$, pure B_r
$i = 45°$, pure B_ϕ
$i = 45°$, pure B_z
$i = 80°$, pure B_r
$i = 80°$, pure B_ϕ
$i = 80°$, pure B_z
100 au
$P = C/C_I$
beam

Figure 3. Heuristic B-vector maps obtained in the same manner as the E-vector map presented in the right panel of Fig. 2, except that the simulated magnetic field is replaced at each point by a single field component: radial (left panels), azimuthal (middle panels) or vertical (right panels). Each of these idealized configurations is shown for three viewing angles: $i = 10°$, $45°$ and $80°$ (top to bottom). Note that the joining of the B-vectors across the mid-plane in the lower right panel is an artefact of the limited resolution of the figure.

3 RESULTS

Before turning to the specific predictions of our model, we present in Fig. 3 synthetic polarization maps for three idealized magnetic field configurations – purely radial (B_r, left panels), purely azimuthal (B_ϕ, middle panels) and purely vertical (B_z, right panels), each shown for three different disc viewing angles – nearly face on ($i = 10°$), nearly edge on ($i = 80°$) and at an intermediate inclination ($i = 45°$; see also Aitken et al. 2002). It is seen that most of the reference configurations exhibit clearly distinguishable polarization patterns. The sole exception arises in the case of edge-on systems, where the basic pattern is the same for both radial and azimuthal field geometries (with the projected magnetic field direction being parallel to the plane of the disc). However, this degeneracy is broken when one takes into account the degree of polarization: in the pure B_ϕ case P peaks at the centre of the projected disc, whereas P is largest near the edges when the field is radial. Another manifestation of this behaviour is seen at intermediate viewing angles: for the pure-B_ϕ case the degree of polarization is maximized on the projected minor axis, whereas for a purely radial field the strongest polarization occurs on the major axis. These trends are readily understood from the expected emission properties of aligned oblate grains (see, e.g. Yang et al. 2016b).

The same three reference field configurations are shown in Fig. 4 for the inferred inclination of the HL Tau disc. In each panel we compare the field orientations inferred from the $> 3\sigma_P$ data (red segments, taken from fig. 1 of Stephens et al. 2014) with the corresponding model predictions (blue segments).[4] This comparison suggests that a primarily vertical field is inconsistent with the observations throughout the disc. Moreover, even though an azimuthal field could in principle be compatible with the data in the central region, it is not possible to match the observed orientations at the edges of the disc's major axis. These inferences are in agreement with the conclusions of Stephens et al. (2014), who found that neither of these two field geometries, nor any combination thereof, provides a good fit to the observations. In contrast, the polarization pattern associated with a radial magnetic field component (left panel) – not explored by Stephens et al. (2014) – appears to be in much better agreement with the data. The observations also indicate a higher degree of polarization away from the disc's minor axis (see fig. 1 of Stephens et al. 2014), which provides further support to the inference of an underlying radial field.

The model described in Section 2 represents a physical realization of a disc in which the radial magnetic field component is dominant. Figure 5 shows the predicted polarization pattern for this model, with the actual data for HL Tau again presented for comparison. As expected on the basis of the preceding discussion, this model provides a fairly good match to the observations. To quantify the goodness of fit, we evaluated the quantity $\epsilon \equiv (\mathrm{RSS}/N)^{1/2}$, where $N = 12$ is the number of data points and RSS is the sum of the squares of the differences between the angular coordinates of the model and the data B-vectors: the smaller the value of ϵ, the better the fit.[5] Applying this measure to the reference cases shown in Fig. 4, we find $\epsilon_{\mathrm{vertical}} = 1.32$, $\epsilon_{\mathrm{azimuthal}} = 0.92$ and $\epsilon_{\mathrm{radial}} = 0.33$, which is consistent with the conclusions we reached on the basis of a visual inspection of the figure. In the case of the wind-driving disc model that we constructed, the presence of a non-negligible azimuthal field component in addition to the (dominant) radial magnetic field endows the polarization pattern with a weak curl whose sense depends on the direction of the disc's rotation. In the absence of additional information about the system, both orientations are possible (corresponding to the projected disc being viewed from either its top or its bottom side), and thus we present both options in the two panels of Fig. 5. In principle, one could use the polarization data to infer the sense of rotation of the underlying disc. In this case, it is not entirely obvious which of the two models provides a better fit: while the clockwise option appears to match a larger number of data points, the counter-clockwise model – even as it matches fewer points – seems to provide a better fit to the ones that it does match. Using our chosen estimator, we find $\epsilon_{\mathrm{counter\text{-}clockwise}} = 0.54$ and $\epsilon_{\mathrm{clockwise}} = 0.34$, which favours clockwise rotation. However, by combining the information on the disc kinematics provided by the HCO^+ channel maps shown in fig. 4 of ALMA Partnership: Brogan et al. (2015) with the [SII] data on the radial velocities in the HL Tau jets shown in fig. 8 of Mundt et al. (1990), we deduce that the HL Tau disc in fact rotates counter-clockwise. This suggests that our simple estimator is not sensitive enough to pick up the correct sense of disc rotation in this source. However, the ϵ value assigned in this scheme to the counter-clockwise model still clearly favours it over models that lack a radial magnetic field component.[6]

While the turbulent magnetic field produced by the MRI mechanism is predominantly azimuthal, it also contains a significant radial component, with the ratio between the mean radial and azimuthal field amplitudes being $\sim$1/3 (e.g. Hawley et al. 1995; Sano & Stone 2002). For comparison, in our numerical disc–wind model, the ratio $|B_r|/|B_\phi|$ along a field line lies in the range $\sim$2–4 (with most of the polarized emission originating near the upper end of this range). To compare the predictions of these scenarios in relation to the HL Tau data, we employ our heuristic model to generate synthetic polarization maps for three combinations

[3] The projected magnetic field vectors – hereafter referred to as B-vectors – are obtained by rotating the electric polarization vectors – hereafter referred to as E-vectors – by 90°. The lengths of the displayed polarization vectors are proportional to the magnitude of P at the projected locations of their centres.

[4] The observed position angle of the HL Tau disc is 138° (measured counter-clockwise from north; ALMA Partnership: Brogan et al. 2015); therefore, to match the horizontal orientation of the major axis of our model disc, we rotated the displayed data clockwise by 48°.

[5] Only the position-angle error (±4.4°) of the central B-vector is reported in Stephens et al. (2014), so we cannot calculate other goodness-of-fit measures, such as the reduced chi-square.

[6] Note that an inherent property of our model is that the relative signs of B_r and B_ϕ at each point are compatible with a magnetic stress that brakes the disc's rotation. Wardle & Königl (1990) used a toy model of a geometrically thin disc that is threaded by a magnetic field possessing an even symmetry with respect to the mid-plane to infer this property directly from the polarization data for the Galactic-centre disc.

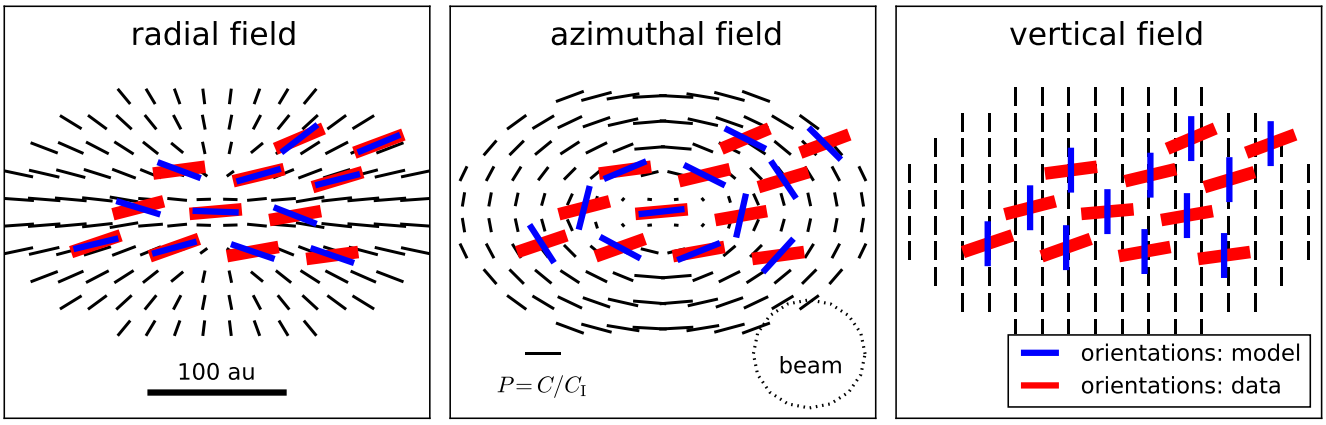

Figure 4. Synthetic polarization maps for the three magnetic field configurations considered in Fig. 3, plotted using the disc viewing angle inferred in HL Tau ($i = 46.7°$). Superposed on the convolved B-vector distributions (black) are the B-vector orientation segments presented by Stephens et al. (2014; red) and the corresponding model predictions (blue).

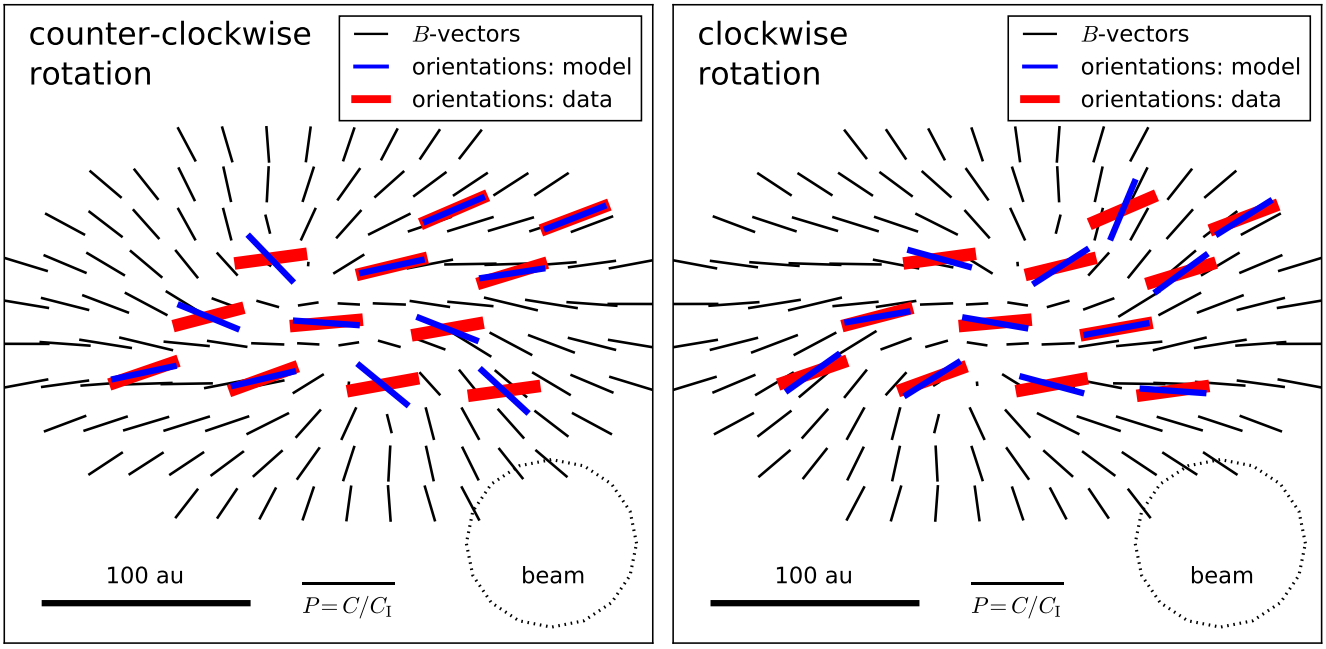

Figure 5. B-vector maps predicted by the simulated wind-driving disc model for counter-clockwise (left) and clockwise (right) disc rotations. The comparison with the data for HL Tau is presented as in Fig. 4.

of radial and azimuthal magnetic fields – corresponding to $|B_r|/|B_\phi| = 1/3$, 1 and 3 – in a counter-clockwise rotating disc (see Fig. 6). The ϵ values obtained for these configurations are $\epsilon_{1/3} = 0.88$, $\epsilon_1 = 0.83$ and $\epsilon_3 = 0.42$. These results indicate that a good fit to the data requires $|B_r|/|B_\phi| \gtrsim 3$, so that, in particular, an MRI disc model cannot account for the observations.

4 DISCUSSION

The numerical model we employed in this paper captures the essential ingredients of a wind-driving disc: sufficiently good field–matter coupling (expressed by the requirement that the Elsasser number Λ be > 1) for the field to develop a radial component, and a sufficiently large field amplitude (corresponding, in the ambipolar diffusivity regime, to the condition $\beta \lesssim 4\Lambda$; see Salmeron et al. 2007) for the magnetic field to be strong enough to drive a CDW. We used this model as a "proof of concept" but did not attempt to optimize the fit by fine-tuning the parameters: this will be done more profitably when data of higher resolution and S/N become available. In addition, real protoplanetary discs are unlikely to have $\Lambda_0 > 1$ and $\beta_0 \gtrsim 1$ at all radial locations as assumed in our model. In general, well-coupled and strongly magnetized models of the type that we employed predict a mean accretion speed that is not much smaller than the local speed of sound, which, in turn, implies a rather short mass depletion time-scale for the disc. Furthermore, there already exists direct evidence for relatively low interior ion-

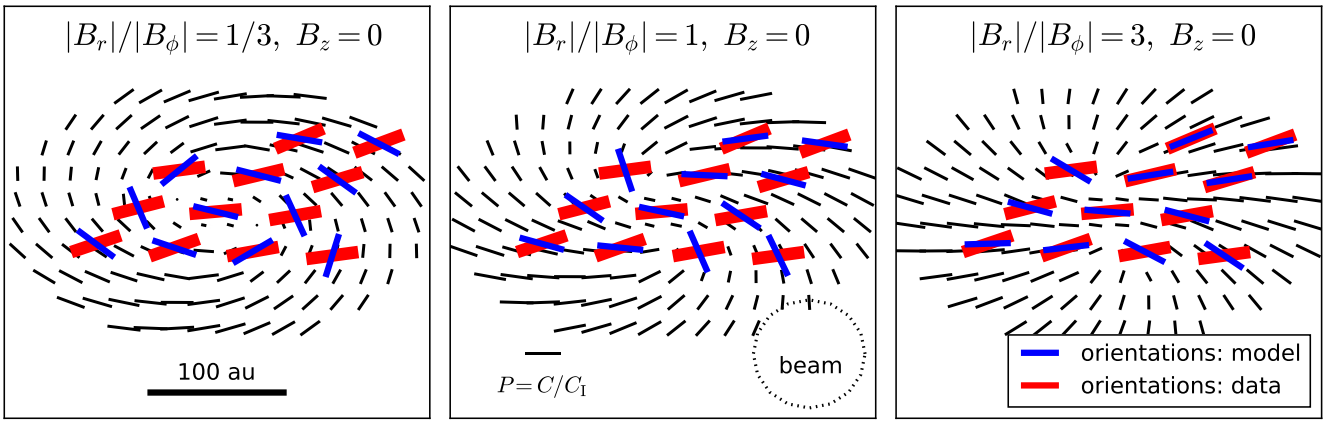

Figure 6. Synthetic polarization maps for three combinations of radial and azimuthal field components, presented in the same format as Fig. 4 under the assumption of counter-clockwise disc rotation.

ization levels in protoplanetary discs on $\gtrsim$10 au scales (e.g. Cleeves et al. 2015), indicating that good coupling may be present only near the disc surfaces. As we noted in Section 1, several numerical models of $\beta_0 \gg 1$ discs that drive winds from comparatively high elevations have already appeared in the literature. However, these models are not yet fully global and thus cannot be used to generate synthetic polarization maps.

As we also already noted in Section 1, the high-β_0 disc models predict that the azimuthal field component should dominate in the vicinity of the mid-plane, implying – if the dust density traces the gas density – that the polarization pattern in HL Tau would resemble that shown in the central panel of Fig. 4 rather than the much better fitting B_r-dominated patterns shown in Fig. 5. In fact, in this source there is direct observational evidence for dust settling to the mid-plane, with the scale height of the mm-wavelength dust disc inferred (from the sharpness of the bright rings in the ALMA image) to be just ∼1 au at a distance of 100 au (Pinte et al. 2016). To be sure, a predominantly azimuthal field geometry is consistent with the polarization maps obtained in some of the other observed sources. One example is the edge-on system L1527, in which Segura-Cox et al. (2015) inferred this geometry from the orientation of the E-vectors (perpendicular to the projected disc plane). This inference is supported by the fact that the measured polarization is strongest near the centre of the disc, which serves to distinguish this configuration from that of a predominantly radial field (see bottom row of Fig. 3). Cox et al. (2015) similarly inferred an azimuthal field geometry in IRAS 4A based on the observed polarization pattern in this source (which, according to Yang et al. 2016b, is viewed at $i \approx 35°$). Indeed, the observed pattern is similar to the one shown in the central panel of Fig. 3, and, in further accord with the synthetic map, the measured degree of polarization peaks along the disc's projected minor axis (most noticeably at 8.1 mm). However, both of these sources are Class-0 objects, in which the observations cannot distinguish between the disc and the inner molecular-cloud envelope. This ambiguity is most pronounced in the case of the third Class-0 source observed to date, the face-on system IRAS 16293-2242B. Rao et al. (2014) identified a spiral magnetic field pattern in the polarization map of this source, which they related to the morphology obtained in a simulation of the collapse of a rotating, magnetized, molecular-cloud core (Padovani et al. 2012). However, in view of the results presented in Fig. 5, it might be possible to interpret this pattern alternatively in terms of a wind-driving disc.

Returning to the case of HL Tau, where the possible contribution of an infalling envelope is not an issue, how can one reconcile the strong indication of a dominant radial field component in the polarization map with the expectation that the bulk of the mm-wavelength emission originates near the disc mid-plane, where the azimuthal field component dominates? One possibility is that the non-negligible optical depth inferred in the bright emission rings of HL Tau at mm wavelengths (Pinte et al. 2016; Jin et al. 2016) shifts the emission centroid to finite disc elevations where the magnetic field already has a measurable radial component. However, in view of the very small scale height inferred for the mm-emitting dust in this source, this is unlikely to be the main explanation. Perhaps a more likely possibility is that, even in this comparatively young source, the grains near the mid-plane, which dominate the total intensity, have already grown to sizes that exceed the maximum size $a_{\rm max} = \lambda/2\pi$ for producing polarized emission at wavelength λ (e.g. Cho & Lazarian 2007; for $\lambda = 1.25$ mm, $a_{\rm max} = 0.2$ mm), while the smaller grains (with sizes $a < a_{\rm max}$), which contribute efficiently to the polarized flux, remain suspended at high elevations (where the field is predominantly radial). Another effect that could lower the polarized emission from grains that have settled to the mid-pane is the likelihood that grains become less elongated as they grow (e.g. Hughes et al. 2009), which would tend to reduce the value of the coefficient C in equation (2) ($C \to 0$ as the grain axis ratio $\to 1$).[7] This interpretation is supported by the finding in the high-resolution observations of IRAS 4A (Cox et al. 2015) of an average polarization of 15% at 8 mm and 10% at 10 mm, with a peak fractional polarization of ∼20%. If the intrinsic degree of mm-wavelength polarization in HL Tau is

[7] A concentration of large grains near the mid-plane would also help explain the sharp contrast between the bright and dark rings in this source (see Ruge et al. 2016).

also of the order of 20% then it may be possible to explain the factor of ∼10 lower value of P measured in this source at 1.25 mm[8] in terms of a dilution of the polarized emission from $a \lesssim 0.1$ mm grains at high disc elevations by weakly polarized emission of larger grains residing near the mid-plane. In this scenario, most of the grains that are responsible for the mm-wavelength flux have settled to the mid-plane and grown to sizes $a \gtrsim 1$ mm.[9] Although a fraction of these grains may have sizes in excess of 1 mm and would therefore emit less efficiently at that wavelength than $a \lesssim 1$ mm grains (e.g. Miyake & Nakagawa 1993), the mid-plane region should still dominate the total mm-wavelength flux if most of the $a \gtrsim 1$ mm grains are concentrated there. Grains of size $a \lesssim 0.1$ mm may be kept at high elevations by turbulent motions that can persist below the wind-driving surface layers (e.g. Simon et al. 2013, 2015; Bai 2015) as well as by the emerging outflows within these layers (see Safier 1993), with porosity effects (e.g. Ormel et al. 2007) possibly also helping to mitigate gravity's pull toward the mid-plane. This scenario of course needs to be backed by detailed calculations and observational tests. One such test would be to obtain a polarization map of HL Tau at longer ($\gtrsim 1$ cm) wavelengths: if the above picture is correct and the grains in the mid-plane region are aligned, such a map could reveal a stronger (or even dominant) contribution from the azimuthal and (especially if $\Lambda_0 \ll 1$) vertical field components.[10] It is, however, conceivable that the large grains in this source are not well aligned because the radiative torque mechanism does not operate efficiently on them: this could happen if the characteristic wavelength of the anisotropic component of the local radiation field were much smaller than the mid-plane grain sizes (e.g. Cho & Lazarian 2007) or if the anisotropic radiation component inside the dust disc were weak due to finite optical-depth effects. Note that the possibility of the mid-plane grains not being well aligned provides another reason for why the polarized mm-wavelength emission from this region could be weak.

A potential caveat to our proposed interpretation arises from the published $\Lambda_0 < 1$, $\beta_0 \gg 1$ numerical disc models cited above, which generally find $|B_\phi|/|B_r| > 1$ in the wind-launching region. A similar behavior is exhibited by the previously obtained $\Lambda_0 < 1$, $\beta_0 \gtrsim 1$ semi-analytic solutions (Li 1996; Wardle 1997), and in both cases it can be understood from the fact that, in the ambipolar diffusion-dominated regime that applies on the $\gtrsim 30$ au radial scales of interest, $|dB_r/dB_\phi|_0 = 2\Lambda_0$ (see Section 2). However, as we have already emphasized, the existing models are not yet fully global, which makes the locally inferred value of $|B_r|/|B_\phi|$ at the base of the wind rather uncertain. Indeed, the magnitudes of the radial and azimuthal field components at the top of the disc are determined by constraints imposed *outside* the disc (e.g. Ogilvie & Livio 2001); in particular, the value of B_r at the base of the wind is related to the magnetic flux distribution interior to the given radial location, whereas the surface value of B_ϕ (which, for a given value of B_z, specifies the magnetic torque that the wind exerts on the disc) is related to the dynamical constraints (imposed at critical points) that a steady-state wind solution must satisfy. It is thus conceivable that a comprehensive, global disc–wind model can be characterized by $|B_r|/|B_\phi| > 1$ at the base of the wind even if this ratio is found to be < 1 in a local approximation. As we inferred in Section 3, this ratio only needs to exceed ∼3 to produce a good fit to the polarization data in HL Tau.

An alternative interpretation of the HL Tau polarization maps in terms of dust scattering of the ambient disc radiation was considered by Kataoka et al. (2015, 2016) and Yang et al. (2016a,b). This mechanism has several distinctive features, although the details of the predicted polarization patterns depend on the shapes, sizes and radiative properties of the grains. In the case of spherical grains, which only contribute to the polarized emission through scattering, Yang et al. (2016a) showed that the predicted polarization structure strongly resembles the one we found in this paper to be associated with emission from aligned grains in a radial magnetic field. In particular, the E-vectors – which, in a disc viewed face on, trace concentric circles – are oriented predominantly along the disc's projected minor axis (with P peaking along the major axis) when $i = 45°$. However, Kataoka et al. (2016) and Yang et al. (2016a) determined that the ∼1% mm-wavelength polarization measured in this source must originate in grains that are much smaller ($a \lesssim 100\,\mu$m) than the mm/cm-size ones inferred to produce the bulk of the emission. This led Yang et al. (2016a) to a suggestion that is very similar to the one that we proposed – on different grounds – in the context of our scenario, namely, that the grains responsible for the polarized emission and the ones from which most of the unpolarized emission originates represent two distinct populations, with the large grains likely concentrated near the mid-plane and the smaller ones probably floating at higher elevations. However, most interstellar dust grains are evidently non-spherical (as first indicated by observations of polarized starlight), so they can become magnetically aligned and produce polarized emission. Yang et al. (2016b) considered both the scattered- and the direct-emission contributions and concluded that, on the spatial scales probed by Stephens et al. (2014), the polarized flux in a source like HL Tau should be dominated by the direct emission component.

Given that purely scattering (spherical) grains produce a polarization pattern that closely resembles that from the direct emission of aligned grains in a radial magnetic field, it could be anticipated that the joint contributions of scattering and direct emission from non-spherical grains in an azimuthal magnetic field might be able to mimic the pattern we obtain in our wind-driving disc model, in which

[8] Stephens et al. (2014) found that P varies across the HL Tau disc between $0.54 \pm 0.13\%$ and $2.4 \pm 0.7\%$, with an average value of 0.90%.

[9] Note that Cox et al. (2015) concluded, based on their inferred upper limit (∼3.2) on the dust spectral index in IRAS 4A, that a large number of mm/cm-size grains are already present in this Class-0 system (see, e.g. Draine 2006). This would suggest that grains with sizes that are at least as big – if not bigger – could form in more evolved (Class-I/II) systems such as HL Tau. The spectral properties of the HL Tau disc are consistent with this picture (e.g. Kwon et al. 2011; Pinte et al. 2016; Carrasco-González et al. 2016).

[10] A 7.0-mm JVLA image of the HL Tau disc with a spatial resolution comparable to that of the 2.9-mm ALMA image (ALMA Partnership: Brogan et al. 2015) was recently obtained by Carrasco-González et al. (2016). The 7.0-mm dust emission was inferred to be optically thin at all radii.

the field has both a radial and an azimuthal component. In particular, it could be expected that this combination would be able to reproduce the spiral magnetic field pattern that is generic to our model and is most pronounced in our synthetic face-on disc maps (see the right panel of Fig. 2). However, as Yang et al. (2016b) pointed out, an oblate grain that is aligned with its minor axis along an azimuthal field will generate a radial E-vector pattern (rather than the azimuthal pattern produced by a spherical grain) when located in the nearly isotropic radiation field that characterizes the inner regions of the disc. Since the direct emission component dominates in the outer disc, the predicted polarization pattern for this case is radial (the same as the direct emission component in an azimuthal field) on all scales. For larger viewing angles, the predicted E-vectors fan out in a "butterfly" pattern, but, again, no spiral structure is produced. This suggests that, if a spiral B-vector pattern such as the one identified in IRAS 16293-2242B (Rao et al. 2014) can be unambiguously associated with a rotationally supported protoplanetary disc, this could serve as a clear discriminant between the two models.

5 CONCLUSION

High-resolution mm- and cm-wavelength polarization maps of protoplanetary discs on scales of $\sim 10^2$ au have recently been obtained for the Class-I/II object HL Tau and for several Class-0 protostars. These maps hold the potential of probing the magnetic field structure and the grain distribution in these discs, as revealed by the thermal emission from aligned dust grains. One of the main results of these observations has been the apparent absence of a significant vertical magnetic field component, which was interpreted as evidence against centrifugally driven winds (CDWs) playing a major role in the angular momentum transport in these discs (e.g. Stephens et al. 2014; Segura-Cox et al. 2015). In this paper we demonstrate, focusing on the case of HL Tau (where, in contrast with the Class-0 systems, there is no doubt that the emission originates exclusively in the disc), that this conclusion need not be true. Using heuristic maps of the polarization patterns produced by single-field-component (radial, azimuthal or vertical) discs as well as synthetic maps generated by post-processing a numerical simulation of a wind-driving disc, we show that the inclusion of a radial field component – which was neglected in the published analyses – significantly improves the fits obtained by using only the azimuthal and vertical field components in modelling the HL Tau data. In fact, we find that the best fit corresponds to a predominantly radial field. Since a strong B_r component is required for launching a CDW and is thus a hallmark of wind-driving discs, we argue that, rather than providing evidence against vertical magnetic angular momentum transport in protoplanetary discs, the polarization maps may in fact corroborate that CDWs are present in these systems. A similar conclusion was previously reached in interpreting the far-infrared polarization map of the pc-scale dust ring in the Galactic centre (Hildebrand et al. 1990, 1993; Wardle & Königl 1990).

The numerical model that we use to demonstrate the basic polarization properties of a wind-driving disc represents a system in which the mid-plane magnetic-to-thermal pressure ratio is relatively large (corresponding to β_0 being not much larger than 1), and in which the field–matter coupling is strong even at $z = 0$ (corresponding to the mid-plane Elsasser number, Λ_0, being > 1). However, real discs may be characterized by $\beta_0 \gg 1$ and possibly also $\Lambda_0 < 1$. In this parameter regime, which numerical simulations have only recently started to explore, disc outflows emerge only above a few thermal-pressure scale heights, and the mid-plane region (where the bulk of the thermal dust emission likely originates) is dominated by the B_ϕ component. To reconcile this structure with our inference of a dominant B_r component in the 1.25-mm polarization map of HL Tau, we suggest that most of the polarized flux originates in $\lesssim 0.1$ mm-size grains that remain suspended above the mid-plane and produce highly polarized ($P \gtrsim 10\%$) emission, and that the grains in the mid-plane region are larger and produce weakly polarized emission at mm wavelengths. (The implicit assumption underlying this proposal – that the B_r component dominates in the surface regions of $\gtrsim 30$ au protoplanetary discs – needs to be verified using global disc–wind models.) One possible (albeit inconclusive) test of this scenario is to search for polarized emission from this source at longer wavelengths: if the grains at the mid-plane region are well aligned, the maps would reveal stronger contributions from the non-radial (B_ϕ and/or B_z) field components.

A recently proposed alternative model (Kataoka et al. 2015, 2016; Yang et al. 2016a,b) attributes the polarization pattern observed in HL Tau to dust scattering of the disc radiation. To be consistent with the spectral emission properties of this source, this model also requires two different grain populations – smaller ones at high elevations and larger ones near the mid-plane – to produce the bulk of the polarized and the total fluxes, respectively. One way to discriminate between the two models would be through the detection of a spiral polarization pattern, like the one identified by Rao et al. (2014) in the Class-0 source IRAS 16293-2242B (where, however, it could not be unambiguously associated with the disc), in a post-Class-0 disc that is viewed at a relatively small angle: such a pattern arises naturally only in the wind-driving disc model.

ACKNOWLEDGEMENTS

We are grateful to Ilsedore Cleeves, Mario Flock, Lynne Hillenbrand, Pat Palmer and John Tobin for fruitful discussions. We also thank the anonymous referee for several very useful comments. This work was supported in part by NASA ATP grant NNX13AH56G and completed with resources provided by the University of Chicago Research Computing Center. This research has made use of NASA's Astrophysics Data System Bibliographic Services and of `matplotlib`, an open-source plotting library for Python (Hunter 2007).

REFERENCES

ALMA Partnership: Brogan et al., 2015, ApJ, 808, L3
Aitken D. K., Efstathiou A., McCall A., Hough J. H., 2002, MNRAS, 329, 647
Bai X.-N., 2013, ApJ, 772, 96
Bai X.-N., 2015, ApJ, 798, 84
Bai X.-N., Stone J. M., 2013, ApJ, 769, 76

Balbus S. A., 2011, in Garcia P. J. V., ed., Physical Processes in Circumstellar Disks around Young Stars. pp 237–282
Bans A., Königl A., 2012, ApJ, 758, 100
Blandford R. D., Payne D. G., 1982, MNRAS, 199, 883
Carrasco-González C., et al., 2016, ApJ, 821, L16
Cho J., Lazarian A., 2007, ApJ, 669, 1085
Cleeves L. I., Bergin E. A., Qi C., Adams F. C., Öberg K. I., 2015, ApJ, 799, 204
Cox E. G., et al., 2015, ApJ, 814, L28
Draine B. T., 2006, ApJ, 636, 1114
Draine B. T., Weingartner J. C., 1996, ApJ, 470, 551
Eardley D. M., Lightman A. P., 1975, ApJ, 200, 187
Ferreira J., Dougados C., Cabrit S., 2006, A&A, 453, 785
Gressel O., Turner N. J., Nelson R. P., McNally C. P., 2015, ApJ, 801, 84
Hawley J. F., Gammie C. F., Balbus S. A., 1995, ApJ, 440, 742
Hennebelle P., Ciardi A., 2009, A&A, 506, L29
Hildebrand R. H., Gonatas D. P., Platt S. R., Wu X. D., Davidson J. A., Werner M. W., Novak G., Morris M., 1990, ApJ, 362, 114
Hildebrand R. H., Davidson J. A., Dotson J., Figer D. F., Novak G., Platt S. R., Tao L., 1993, ApJ, 417, 565
Hughes A. M., Wilner D. J., Cho J., Marrone D. P., Lazarian A., Andrews S. M., Rao R., 2009, ApJ, 704, 1204
Hunter J. D., 2007, Computing In Science & Engineering, 9, 90
Jin S., Li S., Isella A., Li H., Ji J., 2016, preprint, (arXiv:1601.00358)
Kataoka A., et al., 2015, ApJ, 809, 78
Kataoka A., Muto T., Momose M., Tsukagoshi T., Dullemond C. P., 2016, ApJ, 820, 54
Klaassen P. D., Mottram J. C., Maud L. T., Juhasz A., 2016, MNRAS,
Königl A., Salmeron R., 2011, in Garcia P. J. V., ed., Physical Processes in Circumstellar Disks around Young Stars. pp 283–352
Königl A., Salmeron R., Wardle M., 2010, MNRAS, 401, 479
Kwon W., Looney L. W., Mundy L. G., 2011, ApJ, 741, 3
Lesur G., Kunz M. W., Fromang S., 2014, A&A, 566, A56
Li Z.-Y., 1996, ApJ, 465, 855
Looney L. W., Mundy L. G., Welch W. J., 2000, ApJ, 529, 477
Lumbreras A. M., Zapata L. A., 2014, AJ, 147, 72
Mignone A., Bodo G., Massaglia S., Matsakos T., Tesileanu O., Zanni C., Ferrari A., 2007, ApJS, 170, 228
Mignone A., Zanni C., Tzeferacos P., van Straalen B., Colella P., Bodo G., 2012, ApJS, 198, 7
Miyake K., Nakagawa Y., 1993, Icarus, 106, 20
Movsessian T. A., Magakian T. Y., Moiseev A. V., 2012, A&A, 541, A16
Mundt R., Buehrke T., Solf J., Ray T. P., Raga A. C., 1990, A&A, 232, 37
Ogilvie G. I., Livio M., 2001, ApJ, 553, 158
Ormel C. W., Spaans M., Tielens A. G. G. M., 2007, A&A, 461, 215
Padovani M., et al., 2012, A&A, 543, A16
Pinte C., Dent W. R. F., Ménard F., Hales A., Hill T., Cortes P., de Gregorio-Monsalvo I., 2016, ApJ, 816, 25
Rao R., Girart J. M., Lai S.-P., Marrone D. P., 2014, ApJ, 780, L6
Ruge J. P., Flock M., Wolf S., Dzyurkevich N., Fromang S., Henning T., Klahr H., Meheut H., 2016, A&A, 590, A17
Safier P. N., 1993, ApJ, 408, 115
Salmeron R., Königl A., Wardle M., 2007, MNRAS, 375, 177
Sano T., Stone J. M., 2002, ApJ, 577, 534
Segura-Cox D. M., Looney L. W., Stephens I. W., Fernández-López M., Kwon W., Tobin J. J., Li Z.-Y., Crutcher R., 2015, ApJ, 798, L2
Simon J. B., Bai X.-N., Armitage P. J., Stone J. M., Beckwith K., 2013, ApJ, 775, 73
Simon J. B., Lesur G., Kunz M. W., Armitage P. J., 2015, MNRAS, 454, 1117
Stephens I. W., et al., 2014, Nature, 514, 597
Takami M., Beck T. L., Pyo T.-S., McGregor P., Davis C., 2007, ApJ, 670, L33
Tristram K. R. W., Burtscher L., Jaffe W., Meisenheimer K., Hönig S. F., Kishimoto M., Schartmann M., Weigelt G., 2014, A&A, 563, A82
Tzeferacos P., Ferrari A., Mignone A., Zanni C., Bodo G., Massaglia S., 2009, MNRAS, 400, 820
Tzeferacos P., Ferrari A., Mignone A., Zanni C., Bodo G., Massaglia S., 2013, MNRAS, 428, 3151
Wardle M., 1997, in Wickramasinghe D. T., Bicknell G. V., Ferrario L., eds, Astronomical Society of the Pacific Conference Series Vol. 121, IAU Colloq. 163: Accretion Phenomena and Related Outflows. p. 561 (arXiv:astro-ph/9707228)
Wardle M., Koenigl A., 1993, ApJ, 410, 218
Wardle M., Königl A., 1990, ApJ, 362, 120
Yang H., Li Z.-Y., Looney L., Stephens I., 2016a, MNRAS, 456, 2794
Yang H., Li Z.-Y., Looney L. W., Cox E. G., Tobin J., Stephens I. W., Segura-Cox D. M., Harris R. J., 2016b, MNRAS, 460, 4109

This paper has been typeset from a TEX/LATEX file prepared by the author.